Selecting the most relevant brain regions to discriminate Alzheimer's disease patients from healthy controls using multiple kernel learning: A comparison across functional and structural imaging modalities and atlases

Jane Maryam Rondina[a,b,*], Luiz Kobuti Ferreira[a,f], Fabio Luis de Souza Duran[a], Rodrigo Kubo[c], Carla Rachel Ono[c], Claudia Costa Leite[c,d], Jerusa Smid[e], Ricardo Nitrini[e], Carlos Alberto Buchpiguel[c], Geraldo F. Busatto[a,f,g]

[a] Laboratory of Psychiatric Neuroimaging (LIM 21), Department of Psychiatry, Faculty of Medicine, University of São Paulo, São Paulo, Brazil
[b] Sobell Department of Motor Neuroscience and Movement Disorders, Institute of Neurology, University College London, London, UK
[c] Department of Radiology and Oncology, University of São Paulo Medical School, São Paulo, Brazil
[d] Department of Radiology, University of North Carolina at Chapel Hill, NC, USA
[e] Department of Neurology and Cognitive Disorders Reference Center (CEREDIC), University of São Paulo, São Paulo, Brazil
[f] Núcleo de Apoio à Pesquisa em Neurociência Aplicada (NAPNA), University of São Paulo, São Paulo, Brazil
[g] Department and Institute of Psychiatry, University of São Paulo, São Paulo, Brazil

ARTICLE INFO

ABSTRACT

Background: Machine learning techniques such as support vector machine (SVM) have been applied recently in order to accurately classify individuals with neuropsychiatric disorders such as Alzheimer's disease (AD) based on neuroimaging data. However, the multivariate nature of the SVM approach often precludes the identification of the brain regions that contribute most to classification accuracy. Multiple kernel learning (MKL) is a sparse machine learning method that allows the identification of the most relevant sources for the classification. By parcelating the brain into regions of interest (ROI) it is possible to use each ROI as a source to MKL (ROI-MKL).

Methods: We applied MKL to multimodal neuroimaging data in order to: 1) compare the diagnostic performance of ROI-MKL and whole-brain SVM in discriminating patients with AD from demographically matched healthy controls and 2) identify the most relevant brain regions to the classification. We used two atlases (AAL and Brodmann's) to parcelate the brain into ROIs and applied ROI-MKL to structural (T1) MRI, ^{18}F-FDG-PET and regional cerebral blood flow SPECT (rCBF-SPECT) data acquired from the same subjects (20 patients with early AD and 18 controls). In ROI-MKL, each ROI received a weight (ROI-weight) that indicated the region's relevance to the classification. For each ROI, we also calculated whether there was a predominance of voxels indicating decreased or increased regional activity (for ^{18}F-FDG-PET and rCBF-SPECT) or volume (for T1-MRI) in AD patients.

Results: Compared to whole-brain SVM, the ROI-MKL approach resulted in better accuracies (with either atlas) for classification using ^{18}F-FDG-PET (92.5% accuracy for ROI-MKL versus 84% for whole-brain), but not when using rCBF-SPECT or T1-MRI. Although several cortical and subcortical regions contributed to discrimination, high ROI-weights and predominance of hypometabolism and atrophy were identified specially in medial parietal and temporo-limbic cortical regions. Also, the weight of discrimination due to a pattern of increased voxel-weight values in AD individuals was surprisingly high (ranging from approximately 20% to 40% depending on the imaging modality), located mainly in primary sensorimotor and visual cortices and subcortical nuclei.

Conclusion: The MKL-ROI approach highlights the high discriminative weight of a subset of brain regions of

known relevance to AD, the selection of which contributes to increased classification accuracy when applied to ^{18}F-FDG-PET data. Moreover, the MKL-ROI approach demonstrates that brain regions typically spared in mild stages of AD also contribute substantially in the individual discrimination of AD patients from controls.

1. Introduction

Many neuroimaging studies to date have investigated brain abnormalities associated with the diagnosis of Alzheimer's disease (AD), most often using magnetic resonance imaging (MRI), ^{18}F-fluorodeoxyglucose-positron emission tomography (^{18}F-FDG-PET) to measure regional brain metabolism, and single photon emission computed tomography (SPECT) to measure regional cerebral blood flow (rCBF SPECT) (Johnson et al., 2012; Matsuda, 2007; Nordberg et al., 2010; Vemuri et al., 2010). These studies have typically carried out comparisons of mean imaging indices between samples of AD patients and healthy elderly controls across separate brain regions using either regions of interest (ROIs) (Kinkingnéhun et al., 2008; Lehmann et al., 2011; Nadkarni et al., 2012; Ortiz et al., 2014) or voxel-based techniques, applying mass univariate approaches for statistical inference (Kinkingnéhun et al., 2008; Lehmann et al., 2011; Matsuda, 2013). These imaging studies have identified abnormalities in several brain regions in association with the diagnosis of AD from early stages of the disease onwards (Mosconi et al., 2009; Ruan et al., 2016; Thompson et al., 2004). When such traditional mass-univariate approach is used, the detection of the relevance of different brain regions to characterize AD is straightforward; since each ROI or voxel is treated independently, thresholds based on statistical significance and spatial extent can be applied to the statistical parametric results in order to select clusters of voxels with greatest relevance to distinguish AD patients from controls (Ashburner and Friston, 2000; Busatto et al., 2008; Guo et al., 2010; Hirata et al., 2005; Karas et al., 2003).

More recently, a number of neuroimaging investigations of AD have applied machine learning (ML) techniques that allow detection of spatially complex and often subtle neuroimaging patterns of brain abnormalities in individual subjects, building high-dimensional classifiers based on multivariate methods that simultaneously assess multiple voxels within the brain space (Davatzikos et al., 2008; Duara et al., 2013; Klöppel et al., 2008; Ritter et al., 2015; Zhang et al., 2011). Rather than determining statistical group differences, this approach allows classification of images of each subject, providing individual predictions which might ultimately be used in the clinical context (Ferreira and Busatto, 2011; Mcevoy et al., 2009; Petersen et al., 2010; Ruan et al., 2016; Zhang et al., 2011). In contrast with the above mass-univariate strategies, the determination of the most relevant voxels that characterize the difference between groups is not as easily achieved in ML-based approaches, as the weight of each voxel to classify groups depends on all the other voxels, in a multivariate model. In order to address this problem, strategies aiming to select the most relevant voxels to be used as input to the models may be sought to facilitate the interpretation of the weight maps.

In recent years, Multiple Kernel Learning (MKL) approaches have been proposed to combine multiple sources of data in ML algorithms. Up to the present date, the MKL approach has been applied to neuroimaging data predominantly to combine different representations (usually two or more imaging modalities) (Hinrichs et al., 2009; Liu et al., 2014). However, some recent pilot investigations have proposed models in which subsets of features are used as sources of data (Castro et al., 2014; Xia et al., 2014). If these subsets of features are extracted according to some neuroanatomical criterion, it is possible to obtain predictions based on anatomical localization (Mourão-Miranda et al., 2012) and to help to determine which are the most relevant brain regions that contribute to group classification.

In the present study, we aimed to investigate the predictive power of MKL models using ROIs (MKL-ROI) to classify patients with mild AD

versus age- and gender-matched healthy controls, using a multimodal neuroimaging approach comprising morphological MRI, ^{18}F-FDG-PET and rCBF-SPECT data. In contrast with the vast majority of ML-based studies of AD using multimodal imaging designs, we examined exactly the same subjects using the three neuroimaging modalities, with short time intervals between the scanning sessions. We aimed to rank the brain regions affording the greatest degree of discrimination between AD patients and controls according to their contributing weights in each imaging modality, and to establish whether the contribution of each brain region was due to predominantly increased or decreased voxel values in AD patients compared to controls. In addition, diagnostic accuracy indices obtained with the MKL-ROI approach were compared to the indices obtained with Support Vector Machine (SVM) based on the whole-brain. Finally, since recent investigations have suggested that the choice of brain atlas for feature extraction may exert a significant influence on the accuracy of MRI or PET-FDG data in SVM studies of elderly populations (Ota et al., 2014), we compared MKL-ROI results obtained with two different atlases to delineate ROIs, in order to verify the robustness of the accuracies and ranking of weights for each selected brain region.

2. Material and Methods

2.1. Subjects

Thirty-eight individuals were enrolled in this study (20 patients with mild AD and 18 healthy elderly volunteers). The investigation was approved by the ethical committee of the involved institutions and all participants provided informed consent. For both groups, the exclusion criteria were as follows: less than four years of education, age below 60 or above 90 years, use of psychotropic drugs, diabetes mellitus, presence of systemic disorders associated with cognitive decline, contraindications for MRI and brain lesions incidentally detected on MRI.

All patients fulfilled the DSM-III-R (American Psychiatric Association, 1987) and NINCDS/ADRDA (McKhann et al., 1984) criteria for mild dementia and probable AD. Their Clinical Dementia Rating (CDR) scale was lower or equal to 1 (Morris, 1993). As the data were collected before the publication of the new 2011 NINCDS/ADRDA criteria for Alzheimer's disease (McKhann et al., 2011), the criteria for probable Alzheimer's disease from 1984 were used (McKhann et al., 1984).

Healthy controls did not present memory deficits or cognitive impairments (CDR = 0). Table 1 presents age, gender, education and results from Mini Mental State Examination (MMSE) of AD patients and healthy volunteers. Further details regarding the demographic and clinical characteristics of AD subjects and controls can be found in (Buchpiguel et al., 2014).

Table 1
Demographic characteristics of the participants.

	Healthy participants	Patients with AD	*p*-value
Age: mean (SD)	72.7 (4.2)	75.5 (4.0)	0.06
Sex: male (female)	7 (11)	9 (11)	0.70
Education in years: mean (SD)	10.4 (4.8)	7.3 (3.9)	0.05
MMSE: mean (SD)	28.1 (1.3)	21.3 (2.8)	< 0.01

AD – Alzheimer's disease; SD – standard deviation. The *p*-value was obtained using chi-square (for gender) and Mann-Whitney tests (for the continuous variables).

2.2. Image acquisition and pre-processing

2.2.1. T1 Magnetic Resonance Imaging (T1-MRI)

Spin echo T1-weighted images were obtained on the sagittal plane with the following parameters: TR 12.1, TE 4.1999, flip angle 15°, pixel bandwidth 88.75, matrix 256 × 256, voxel size 0.86 × 0.86 × 1.6 mm, 204 slices, slice thickness 1.6. These images were acquired using a General Electric-Horizon LX 8.3 1.5 Tesla scanner (Milwaukee, WI, USA).

Non-brain tissues were removed from the T1-MRI anatomical images applying the Hybrid Watershed algorithm (Ségonne et al., 2004), implemented in Freesurfer v.3.04 (Athinoula A. Martinos Center for Biomedical Imaging, Massachusetts, USA; http://surfer.nmr.mgh. harvard.edu). The N3 algorithm, (Sled et al., 1998) also implemented in Freesurfer, was used to perform intensity normalization. The Brain Extraction Tool (Smith, 2002) implemented in FSL (Oxford's Functional MRI Software of the Brain Library, UK; www.fmrib.ox.ac.uk/fsl) was used to perform a final non-brain tissue removal (Pereira et al., 2010).

Images were then segmented into gray matter (GM) and white matter partitions using the unified segmentation procedure (Ashburner and Friston, 2005) as implemented in SPM8 (Statistical Parametric Mapping software, version 8; http://www.fil.ion.ucl.ac.uk/spm; Well-come Department of Imaging Neuroscience, London). The segmented images were spatially normalized to the standard MNI space using the Diffeomorphic Anatomical Registration Through Exponentiated Lie Algebra (DARTEL) algorithm (Ashburner, 2007). This procedure maximizes the sensitivity and accuracy of localization by registering individual structural images to an asymmetric custom T1-weighted template derived from the participants' structural images rather than to a standard T1-weighted template based on a different sample (Curiati et al., 2011). The normalized GM images were resliced with trilinear interpolation to a final voxel size of $2 \times 2 \times 2$ mm^3. An additional procedure was performed to modulate the images, consisting of multiplying each spatially normalized GM image by its relative volume before and after normalization; this ensured that the total amount of GM in each voxel was preserved. Finally, the resulting GM images were smoothed using an 8 mm isotropic kernel at full width half maximum (FWHM).

2.2.2. Positron Emission Tomography (PET)

All subjects had blood glucose levels determined in the beginning of the PET scanning session. After a period of at least 6 h of fasting, they received 370 MBq of [18F] fluoro-2-D-deoxyglucose (FDG). Imaging started 60 min after FDG administration, using a 3-D protocol with acquisition time of 15 min. The acquisition was performed using a dedicated LSO-PET 16-slice CT scanner (Biograph-16, Siemens, Illinois-USA). The matrix size was 256 × 256 with a smoothing factor of 5. Iterative reconstruction (OSEM) was applied according to a standardized protocol in our institution. Attenuation was corrected using the CT-algorithm.

^{18}F-FDG-PET images were coregistered to the skull striped T1-MRI in its native space using SPM8. Partial volume effects (PVE) correction was applied to the coregistered images to avoid confounding effects related to regional brain atrophy (Curiati et al., 2011). The Meltzer method (Meltzer et al., 2000), a voxel-based PVE correction algorithm implemented in the PVElab software (http://nru.dk/downloads/software) (Quarantelli et al., 2004) was applied.

The spatial transformation parameters resulting from the T1-MRI normalization steps (described above) were applied to ^{18}F-FDG-PET images in order to achieve spatial normalization to the standard MNI space. The normalized images were smoothed with a Gaussian filter of 8 mm at FWHM. Normalization of images to the global tracer uptake was performed by dividing the value of each voxel by the average of all voxels belonging to a whole-brain mask.

2.2.3. Single Photon Emission Computed Tomography (SPECT)

The subjects received IV injection of 20 mCi (740 MBq) of [99mTc]-ECD 30 min before the images acquisition. A dual-detector SPECT camera equipped with a fan beam collimator (ECAM, Siemens, Hoffmann Estates, Illinois) was used. SPECT images were processed according to a standard protocol, with no attenuation correction and a Butterworth post filtering. The reconstruction yielded 4.8 mm voxels with a 128 × 128 matrix and 128 slices. In-plane spatial resolution was 10.6/6.7 mm full width at a half maximum (FWHM) in the center of view. Images were reconstructed with scatter correction. The rCBF-SPECT images were also coregistered to the skull striped T1-MRI in its native space using SPM8 and corrected for PVE using the Meltzer as described for the ^{18}F-FDG-PET data (Meltzer et al., 2000).

Spatial normalization using transformation parameters resulting from the T1-MRI data, Gaussian smoothing (8 mm at FWHM) and normalization to global tracer uptake were conducted using the same methods described above for the ^{18}F-FDG-PET data.

2.3. Classification techniques

In supervised learning, classification corresponds to the task of identifying to which of a set of categories a new example belongs, based on a training set of data containing examples whose membership is previously known.

2.3.1. Learning from a single source

Individual examples are often represented by a set of quantifiable properties, known as explanatory variables or features. These properties may be categorical, ordinal, integer-valued or real-valued (e.g. a measurement of intensity of voxels in brain images). Thus, a source of information can be represented by a data matrix X composed by n examples and p features. In neuroimaging-based classification, each feature may correspond to a single voxel and each example may correspond to an anatomical scan from a single subject, for example. Many classifiers work by comparing examples by means of a similarity or distance function (*kernels*). A function is used to build kernel matrices, whose dimensions correspond to the number of examples. In our analyses, we applied a linear kernel given by the scalar product of the data matrix:

$$K = X \bullet X^T \tag{1}$$

In a binary classification (2 classes), the examples (e.g. images from each subject $x_i \in R^n$) are associated to labels y_i, which can assume one of two possible values (-1 or 1).

In this study, we used SVM (Boser et al., 1992; Vapnik, 1998) to classify AD patients and healthy controls. The linear SVM is defined as an optimization problem that can be represented through a dual formulation, where n is the number of training examples, α_i is the contribution of the *i-th* training example to the final solution, y_i is the label of the *i-th* training example and C is a regularization parameter that controls the distance between the hyperplane and the support vectors.

$$\max_{\alpha_i} \quad -\frac{1}{2}\sum_{i,j}^{n} y_i y_j \vec{x_i} \cdot \vec{x_j} \alpha_i \alpha_j + \sum_{i=1}^{n} \alpha_i \tag{2}$$

$$such\ that\ \sum_{i=1}^{n} \alpha_i y_i = 0\ and\ 0 \leq \alpha_i \leq C \tag{3}$$

Once this equation is solved, α_i and b are determined and can be used to classify a test example $\vec{x}$ based on the following equation, which classifies $\vec{x}$ as either 1 or -1.

$$f(\vec{x}) = sign\left[\sum_{i=1}^{n} \alpha_i y_i K(\vec{x_i}, \vec{x}) - b\right] \tag{4}$$

We fixed the regularization parameter C at the value 1 in all analyses, as our aim was not to maximize the accuracy, but instead to

provide a comparison across modalities and atlases using ROI-based MKL.

2.3.2. Learning from multiple sources

With the growing application of ML models based on neuroimaging in neuroscience and clinical investigations, a topic that becomes increasingly relevant is interpretability (i.e. which areas of the brain mostly contribute to the predictions provided by the models). In a clinical application, this information can provide insights about how a psychiatric or neurologic disorder affects the brain (Mourão-Miranda et al., 2012). However, since the prediction is based on a multivariate pattern, all features given as input to the model contribute to generate a predictive function. The issue of model interpretability is particularly relevant when using algorithms that have non-sparse weights associated to the features, as in the case of SVM (Rondina et al., 2013).

In neuroimaging, different data sources may comprise different imaging modalities (e.g., T1-MRI or FDG-PET), different ways of extracting data from a same modality (e.g., volumetric or cortical thickness in structural MRI), or different feature subsets. In the present study, we are interested in the latter approach (i.e., using feature subsets as kernels and combining them). We are particularly interested in investigating models based on subsets of features extracted according to anatomical criteria, in order to obtain predictions that are meaningful in regard to anatomical localization. We use the acronym MKL-ROI throughout the text to represent this approach (distinguishing it from other potential uses of MKL methods to combine other kinds of sources of data).

2.3.2.1. Multi-Kernel Learning (MKL).
Kernel methods can operate on very general types of data and can detect different types of relations. Thus, they provide a natural way to merge and integrate different sources of information. Recent applications have shown that using multiple kernels instead of a single one can enhance the interpretability of the decision function, and in some cases improve the final performance. A convenient approach is to consider that the kernel $K(x, x')$ is actually a convex combination of *basis* kernels (Lanckriet et al., 2004):

$$K(x, x') = \sum_{m=1}^{M} d_m K_m(x, x'), \text{ with } d_m \geq 0, \sum_{m=1}^{M} d_m = 1 \qquad (5)$$

In Eq. (5) M is the total number of kernels. Within this framework, the problem of data representation through the kernel is transferred to the choice of weights d_m. Learning both the coefficients i and the weights d_m in a single optimization problem is known as the MKL problem. In the current investigation, we applied the algorithm SimpleMKL (Rakotomamonjy et al., 2008) available in the toolbox PRoNTo (Schrouff et al., 2013).

SimpleMKL consists in optimizing problems addressed by SVM by computing an optimal weighting. The minimization problem includes a constraint on the *L1* norm of the vector *d*, which induces sparsity in the solution. This property allows the model to keep only the most relevant patterns in the kernel computation. The SimpleMKL problem is solved by alternating a classical SVM together with a projected gradient descendent according to vector *d*, allowing to minimize the objective function while ensuring that constraints on vector *d* are fulfilled. The *L-norm* constraint on the vector *d* is a sparsity parameter that forces some kernels to have zero weight, thus encouraging sparse basis kernel expansions. The mixed-norm (L1 and L2) penalization of $d_m K_m(x, x')$ is a soft-thresholding penalizer that leads to a sparse solution, for which the algorithm performs kernel selection. Thus, the procedure to find the number of selected kernels (ROIs) is based on Gradient descent (Mandic, 2004), that minimizes a cost function aiming the minimum error in fitting parameters to the training data.

2.3.2.2. ROI-based MKL.
In this study, we are interested in

investigating the anatomical localization of the features that contribute the most to classify AD patients and healthy controls. Thus, we applied an MKL approach in which each data source corresponds to subsets of the features in the brain. To obtain subsets of voxels with anatomical meaning we used parcellation templates (brain atlases) to provide ROIs.

In order to investigate to what extent different criteria of anatomical segmentation affect the MKL-ROI performance, we carried out separate analyses using two atlases: Automated Anatomical Labeling (AAL) atlas (Tzourio-Mazoyer et al., 2002) and Brodmann's Areas (BA) atlas (Brodmann, 1909) furnished by the software MRICRO (Rorden and Brett, 2000). Regions belonging to the cerebellum were not included, as the effect of AD neuropathology on this area is thought to be minimal, at least in the early stages of the disease (Fox et al., 2001; Minoshima et al., 1997). Each structure in the AAL atlas is associated to two ROIs (in the left and right hemispheres); on the other hand, the BA atlas encompasses bilateral regions. Therefore, in order to make the two atlases more comparable with each other, we merged the left and right regions for each structure in the AAL atlas into a single ROI. Thus, we worked with 45 regions from the AAL atlas and 48 regions from the BA atlas. However, the number of selected regions varies across the analyses reported, due to the fact that the SimpleMKL is a sparse method (i.e., null weight is assigned to several kernels during the learning process).

Fig. 1 illustrates the framework of the MKL-ROI approach. The atlas provides anatomical ROIs, represented in colours in the figure. Each ROI is defined by a disjoint set of voxels with unique indices in a standard three-dimensional space. As the features correspond to individual voxels, each ROI is considered a features set (represented by F_1 to F_M in the figure). Voxels in the training images from both groups (patients and healthy controls) corresponding to the indices of each ROI compose the kernel matrices (K_1 to K_M). They encode similarity measures of each pair of examples (images from each training subject limited by a mask defined by the particular ROI). The SimpleMKL algorithm optimizes the weights of each kernel in a sparse way, so that only a subset of kernels have non-zero weight in the learned classification function (f_{MKL} in the figure). The complete process is performed inside a cross-validation loop. Thus, after all iterations, a set of selected ROIs and their respective weights is obtained. Additionally, as each voxel correspond to a particular feature, the voxels belonging to the selected ROIs are also associated to individual weights. This concept is more formally detailed in Section 2.5, where we define the terms 'ROI-weight' and 'voxel-weight', which will be important to evaluate the predominance of hypometabolism/atrophy or hypermetabolism/hypertrophy for each region in a subsequent analysis.

2.4. Validation

The predictive performance for each method is given by the balanced average (BA) between the proportions of true positive (TP) and true negative (TN) (i.e. patients and controls correctly classified, respectively).

We used cross-validation to assess how the results of the classification analyses could generalize to an independent data set. One round of cross-validation involves partitioning the data sample into disjoint subsets of examples, performing the analysis on one subset (the training set), and validating the analysis on the other subset (the validation or testing set). To reduce variability, multiple rounds of cross-validation are performed using different partitions, and the validation results are averaged over the rounds. In the present study, we used a leave-one-subject-out cross-validation (LOO-CV), which involves separating a single example (either patient or control) from the complete sample for test while the remaining examples are used for training. This splitting is repeated so that each example in the whole sample is used once for validation. After all iterations, the final accuracy is quantified as the average of accuracies obtained across all folds. The balanced accuracy
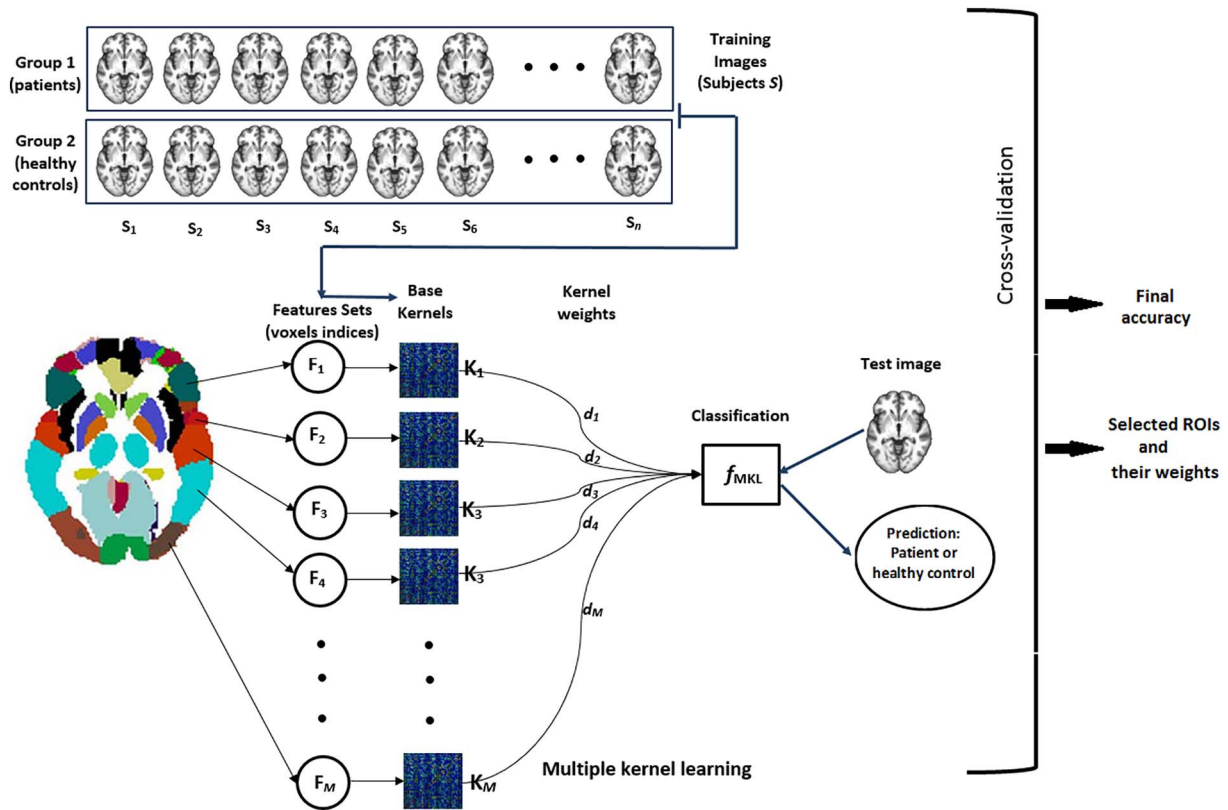
Fig. 1. MKL-ROI framework. The atlas consists of anatomical ROIs represented in different colours. Each ROI is defined by a disjoint set of voxels with unique indices in a standard three-dimensional space. These are subsets of voxels (features) represented by F_1 to F_M. The training images from both groups (patients and healthy controls) limited by the indices of each ROI compose each kernel matrix (K_1 to K_M). The SimpleMKL algorithm optimizes the weights of each kernel in a sparse way, so that only a subset of kernels have non-zero weight in the classification function (f_{MKL}). The complete process is performed inside a cross-validation loop, resulting in a list of selected (non-zero) ROIs, from which the final accuracy is obtained.

is computed from a set of class-specific accuracies, taking the number of samples in each class into account.

To evaluate whether the resulting classification accuracy is statistically significant, we used a permutation test with 10,000 repetitions. In this non-parametrical test, the labels are randomly permuted across examples and the classification procedure is repeated a high number of times. The probability of having obtained the result by chance is given by the count of the number of instances when the classification with permuted labels outperforms the original classification (with the correct labels). This count is divided by the number of repetitions to obtain a percentage value p.

2.5. Weights in selected brain regions

As both coefficients α_i and d_m are learnt in a single optimization problem (linear eqs. (4) and (5)), besides the weight associated to each kernel, the weight of each feature in the selected regions can also be recovered. For clarity of presentation, from now on we will refer to the weight assigned to each kernel as 'ROI-weight' and to the weight assigned to each feature as 'voxel-weight'. In the training of the classifier, the label $+1$ was assigned to the class corresponding to the AD group and the label -1 was assigned to the healthy control group. Thus, a positive voxel-weight indicates relatively higher radiotracer uptake (PET and SPECT data) or increased GM volume (T1-MRI) in the AD group when compared to the healthy control group whereas a negative voxel-weight indicates higher radiotracer uptake or increased GM volume in the healthy control group for the particular location.

For each ROI we wanted to characterize if the predominant type of changes were related to either hypometabolism/atrophy or hypermetabolism/structural preservation. Thus we calculated the ratio between positive and negative voxel-weights within each selected ROI,

performing the following steps:

1. Obtained the probability density function of the voxel-weight vector;
2. Calculated the area under curve separately for negative and positive voxel-weights ($AUC-$ and $AUC+$, respectively);
3. Obtained the ratio $rAUC = AUC-/AUC+$.

Using $rAUC$ we characterized the selected ROIs according to the predominance of signal: regions for which $rAUC$ was close to 1 were considered to be mixed (i.e. balanced positive and negative voxel-weights). Values close to zero suggest regions that have predominantly positive voxel-weights and values higher than one suggest regions that have predominantly negative voxel-weights.

3. Results

3.1. Classification performance across modalities and atlases

In this section we present the performance of the classification of AD patients and healthy controls for all modalities using whole-brain SVM (Table 2a) and using MKL-ROI with both atlases considered: AAL (Table 2b) and BA (Table 2c). For each analysis we present the balanced accuracy, the sensitivity (described as true positive - the proportion of patients correctly classified) and the specificity (described as true negative – the proportion of healthy controls correctly classified).

For the whole-brain SVM analyses, similar accuracies were obtained using ^{18}F-FDG-PET (84.17%) and rCBF-SPECT (81.94%). Using T1-MRI, the accuracy was lower (73.89%) in comparison with both functional modalities.

For MKL-ROI analyses, the best accuracy was obtained with ^{18}F-

Table 2
Classification results.

Modality	NSR	NF	TP	TN	BA	p
T1-MRI	–	219,727	70.00%	77.78%	73.89%	0.013
^{18}F–FDG-PET	–	219,727	85.00%	83.33%	84.17%	< 0.001
rCBF-SPECT	–	219,727	75.00%	88.89%	81.94%	< 0.001
(a) SVM (Whole-brain)						
T1-MRI	20	64,605	80.00%	72.22%	76.11%	0.016
^{18}F–FDG-PET	23	71,673	85.00%	100.00%	92.50%	< 0.001
rCBF-SPECT	18	59,286	85.00%	83.33%	84.17%	< 0.001
(b) MKL-ROI (AAL atlas)						
T1-MRI	19	66,111	70.00%	66.67%	68.33%	0.080
^{18}F–FDG-PET	21	64,197	85.00%	100.00%	92.50%	< 0.001
rCBF-SPECT	17	58,975	70.00%	77.78%	73.89%	0.018
(c) MKL-ROI (BA atlas)						

T1-MRI: T1-weighted magnetic resonance imaging; ^{18}F-FDG-PET: ^{18}F-fluorodeoxyglucose-positron emission tomography; rCBF-SPECT: regional cerebral blood flow single photon emission computed tomography; NSR: Number of selected ROIs (assigned non-zero ROI-weight); NF: number of features (voxels) in the set of selected ROIs; TP: true positive (percentage of patients correctly classified); TN: true negative (percentage of healthy controls correctly classified); BA: balanced accuracy; p: statistical significance given by permutation.

FDG-PET, followed by rCBF-SPECT and T1-MRI for both atlases. For ^{18}F-FDG-PET, the accuracy obtained with the BA atlas was the same as the accuracy obtained with AAL atlas (92.50%). Conversely, for both T1-MRI and rCBF-SPECT, the accuracy obtained with AAL atlas was higher than the accuracy obtained with the BA atlas (respectively 76.11% versus 68.33% for T1-MRI, and 84.17% versus 73.89% for rCBF-SPECT) (Tables 2b and 2c).

The number of selected ROIs (NSR) was slightly higher for the AAL atlas than for the BA atlas in the three modalities, although the actual number of features used as input for the MKL-ROI models (NF) varies across them. It is interesting to notice that even though the accuracies resulting from MKL-ROI analyses with AAL atlas was higher than the accuracies obtained using whole-brain SVM for all modalities, the number of selected ROIs was considerably low. Out of 45 ROIs, 20 were selected in T1-MRI, 23 in ^{18}F-FDG-PET and 18 in rCBF-SPECT, corresponding to respectively 29%, 33% and 27% of the total number of voxels. For the BA atlas, out of 48 ROIs, 19 were selected on T1-MRI, 21 on ^{18}F-FDG-PET and 17 on rCBF-SPECT, corresponding to respectively 30%, 29% and 27% of the total number of voxels. These results show that the models are substantially sparse, providing good accuracy indices using only the most relevant features.

In Fig. 2 we show the Receiver Operating Characteristic (ROC) curves (plots of the true positive rate against the false positive rate for the different possible cut points) for each analysis presented in Table 2. Plots (a)–(c) were derived from SVM using the whole-brain for T1-MRI, FDG-PET and rCBF-SPECT, respectively. Plots (d)–(f) were derived from MKL-ROI using the Brodmann atlas and plots (g)–(i) were derived from MKL-ROI using the Brodmann atlas. The area under curve (AUC) is presented in each plot.

3.2. Selected brain regions and relevance

In Tables 3 and 4, we present the brain regions which were selected by MKL-ROI to classify AD patients and healthy controls using the AAL and BA atlases, respectively. For each modality (T1-MRI, ^{18}F-FDG-PET and CBF-SPECT), the selected ROIs were sorted in descending order of ROI-weight.

In the analyses using the AAL atlas (Table 3), although several cortical and subcortical regions contributed to the discrimination between AD patients and controls, highly prominent ROI-weights were

detected in: the posterior cingulate gyrus (around 30% of the total ROI-weight), fusiform gyrus and cuneus (around 15% each) for PET; the posterior cingulate gyrus (around 25%), fusiform gyrus and angular gyrus (around 20% each) for SPECT; and the inferior temporal gyrus and caudate nucleus (both around 20%) for T1-MRI (Table 3). In the analyses using the BA atlas, a similar pattern involving several brain foci but with greater emphasis on a few selected regions emerged (Table 4). However, there were differences in regard to brain location and attributed ROI-weights relative to the analyses using the AAL atlas, with greatest ROI-weights detected in: the medial parietal cortex (around 35%) and parahippocampal gyrus (around 15%) for PET; the medial parietal cortex (around 25%), secondary visual cortex (around 20%) and posterior cingulate gyrus (around 15%) for SPECT; and entorhinal cortex, posterior cingulate gyrus, inferior and auditory temporal gyri (each around 15% of the total ROI-weight) for T1-MRI (Table 4).

The data presented in Tables 3 and 4 also provide the description of brain regions in which voxels with lower or higher values predominated in AD patients relative to controls (as ascertained by the ratio between positive and negative voxel-weights within each ROI - rAUC). These analyses demonstrated that for the three imaging modalities, most regions presented rAUC above 1, indicating a predominant pattern of hypometabolism/atrophy. A number of brain regions presented rAUC values below 1; thus the ROI-weight of discrimination in these regions was mostly due to a pattern of increased (rather than decreased) voxel-weight values in AD individuals, indicating relative hypermetabolism/structural preservation in AD patients relative to controls. Most of the ROIs that presented such pattern encompass brain regions typically spared in mild stages of AD, including: the visual cortex, primary motor and somatosensory cortices, subcortical nuclei (caudate, putamen, pallidum and thalamus) and orbitofrontal cortex (Tables 3 and 4).

Fig. 3 and Fig. 4 illustrate the selected brain regions in colours according to the ROI-weight assigned to them by the MKL-ROI classification using the AAL and BA atlases respectively. Each modality is shown in a separate panel: T1-MRI (Fig. 3a and Fig. 4a); ^{18}F–FDG-PET (Fig. 3b and Fig. 4b) and rCBF-SPECT (Fig. 3c and Fig. 4c).

Fig. 5 presents examples of voxel-weights within ROIs BA7 and BA37 to illustrate the heterogeneity of the regions regarding the signal of weights assigned to each feature as well as the presence of spatial clusters of similar weights.

Fig. 6 and Fig. 7 present the predominance of positive and negative signal in the voxel-weights of each ROI selected using the AAL and BA atlases, respectively. The colour in each region represents the rAUC. Cool colours represent predominance of hypometabolism/atrophy in AD patients while warm colours indicate relative hypermetabolism/structural preservation.

4. Discussion

To the best of our knowledge, the present study is the first to compare the diagnostic performance of two different SVM approaches (MKL-ROI-based and whole-brain-based) to discriminate patients with mild AD from age- and gender-matched healthy controls using multimodal neuroimaging data acquired in exactly the same subjects with short inter-scanning intervals. The use of the MKL-ROI approach to rank brain regions allowed us to highlight the foci with greatest discriminating ROI-weight to distinguish AD patients from healthy controls across the three imaging modalities employed (T1-MRI, ^{18}F-FDG-PET and rCBF SPECT), with analyses repeated using two different brain atlases.

Regardless of the atlas employed, the MKL-ROI analysis of PET data indicated highest discriminating ROI-weight afforded by medially located posterior cortical regions (medial parietal cortex encompassing the precuneus and posterior cingulate gyrus). This pattern of results is highly consistent with the findings of previous functional imaging studies that conducted statistical group comparisons or visual
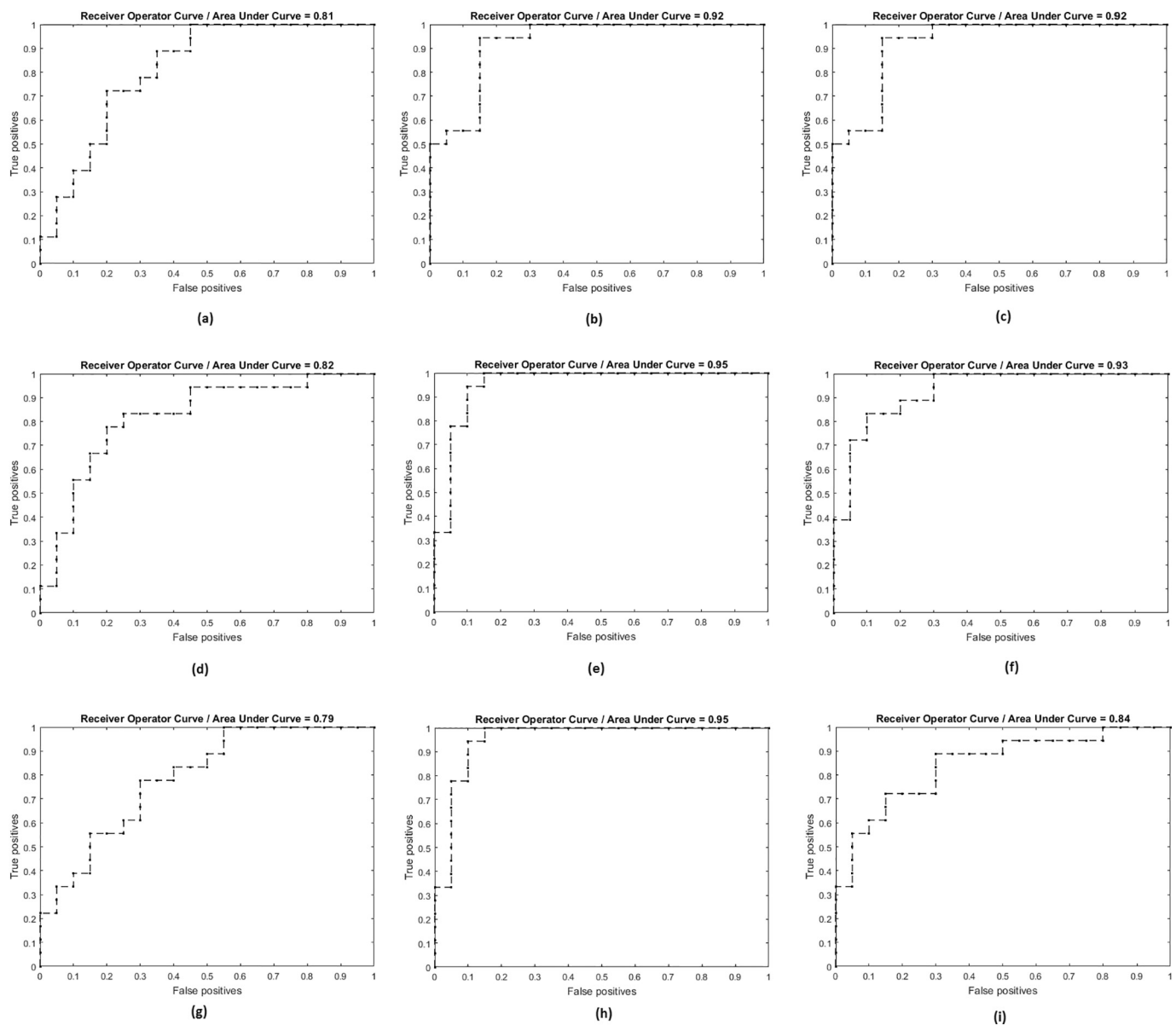
Fig. 2. ROC curves. (a) Whole-brain-based SVM using T1-MRI; (b) Whole-brain-based SVM using FDG-PET; (c) Whole-brain-based SVM using rCBF-SPECT; (d) AAL-based MKL-ROI using T1-MRI; (e) AAL-based MKL-ROI using FDG-PET; (f) AAL-based MKL-ROI using rCBF-SPECT; (g) Brodmann-based MKL-ROI using T1-MRI; (h) Brodmann-based MKL-ROI using FDG-PET; (i) Brodmann-based MKL-ROI using rCBF-SPECT.

inspection of individual PET data from patients suffering from AD or amnestic mild cognitive impairment (MCI) compared to elderly controls; these investigations have highlighted the relevance of metabolic hypoactivity in the posterior cingulate gyrus (BA 23) and medial parietal cortex (BA 7) among the most characteristic features of the prodromal phase of AD and early stages of dementia (Ishii, 2014; Minoshima et al., 1997; Mosconi et al., 2010; Silverman, 2004). It is relevant to note that these brain regions alone were responsible for approximately 25% and 40% (using the AAL and BA atlases, respectively) of the ROI-weight of discrimination between AD patients and controls in our MKL-ROI analysis of PET data. Our results indicate that such localized foci of brain hypoactivity have very strong voxel-weight in the discrimination between patients with early AD and elderly controls when SVM-based methods are applied to PET data. It is widely known that local molecular and neuropathological changes and disconnection patterns that characterize AD may begin several years before any cognitive deficits emerge (Delacourte et al., 1999; Morris et al., 1996), slowly progressing in a spreading fashion across cortical and

subcortical brain regions (Braak and Braak, 1991; Delacourte et al., 1999). Our PET findings reinforce the view that the macroscopic brain metabolic patterns that most critically typify the probable diagnosis of AD on an individual basis remain relatively localized even when clear symptoms of dementia are already present. By highlighting the same brain regions emphasized in previous studies investigating the clinical utility of ^{18}F-FDG-PET data to allow diagnostic predictions in individual elderly subjects (Ishii, 2014), our findings strengthen the potential usefulness of ML-based approaches in clinical practice.

When comparing the MKL-ROI-based findings obtained with SPECT with the results of the same analysis using PET data, we found a considerable degree of coincidence in regard to the brain regions that had the largest ROI-weight of discrimination between AD patients and healthy controls between the two functional imaging modalities, particularly in regard to medially located posterior cortical regions (medial parietal cortex encompassing the precuneus and posterior cingulate gyrus). Taking into account the results based on the BA atlas, there was also concordance in the MKL-ROI-based analysis of PET and SPECT data

Table 3
Regions from AAL atlas selected by MKL-ROI to classify AD patients and healthy controls.

	T1-MRI			¹⁸F-FDG-PET			CBF-SPECT		
	ROI	ROI-weight (%)	rAUC	ROI	ROI-weight (%)	rAUC	ROI	ROI-weight (%)	rAUC
1	Inf. temporal gyrus	22.344	6.37	Posterior cingulate gyrus	31.238	2.03	Posterior cingulate gyrus	26.882	3.63
2	Caudate nucleus	19.379	0.89	Fusiform gyrus	15.398	3.15	Fusiform gyrus	22.680	1.08
3	Paracentral lobule	11.489	0.04	Cuneus	14.148	1.09	Angular gyrus	20.796	9.73
4	Sup. temporal pole	9.595	0.22	Medial frontal gyrus	10.524	12.48	Hippocampus	11.655	4.38
5	Posterior cingulate gyrus	9.029	22.28	Globus pallidus	8.848	0.05	Lingual gyrus	10.014	0.41
6	Amygdala	7.948	8.96	Angular gyrus	7.499	3.83	Precuneus	3.186	4.82
7	Sup. temporal gyrus	6.575	1.18	Sup. parietal lobule	5.693	1.01	Globus pallidus	2.343	0.09
8	Inf. frontal gyrus, pars orb.	4.339	1.81	Olfactory cortex	2.742	51.61	Postcentral gyrus	1.070	0.30
9	Medial orbitofrontal cortex	3.071	0.25	Thalamus	1.680	0.47	Sup. parietal lobule	0.444	1.25
10	Inf. parietal lobule	2.332	3.37	Paracentral lobule	0.528	0.15	Cuneus	0.340	1.04
11	Postcentral gyrus	1.444	0.94	Hippocampus	0.487	2.23	Inf. frontal gyrus, pars tri.	0.177	3.26
12	Precuneus	0.741	2.46	Precuneus	0.323	2.48	Paracentral lobule	0.122	0.10
13	Middle frontal gyrus	0.541	2.09	Calcarine sulcus	0.262	0.23	Medial frontal gyrus	0.100	6.10
14	Transverse temporal gyrus	0.522	7.69	Insula	0.164	2.02	Amygdala	0.066	0.51
15	Sup. frontal gyrus, orbital part	0.258	3.27	Middle occipital gyrus	0.103	1.02	Transverse temporal gyrus	0.046	9.52
16	Inf. frontal gyrus, pars tri.	0.230	1.74	Rolandic operculum	0.098	0.70	Putamen	0.046	0.26
17	Middle occipital gyrus	0.074	3.07	Gyrus rectus	0.085	11.66	Middle occipital gyrus	0.033	1.65
18	Thalamus	0.072	2.69	Middle temporal gyrus	0.067	3.20	Sup. frontal gyrus	0.001	2.37
19	Sup. Occipital	0.015	3.77	Inf. frontal gyrus, pars tri.	0.049	7.40			
20	Inf. occipital cortex	0.003	3.15	Medial orbitofrontal cortex	0.024	3.64			
21				Inf. frontal gyrus, pars orb.	0.023	5.61			
22				Midcingulate area	0.011	1.86			
23				Parahippocampal gyrus	0.004	7.82			

T1-MRI: T1-weighted magnetic resonance imaging; ¹⁸F-FDG-PET: ¹⁸F-fluorodeoxyglucose-positron emission tomography; rCBF SPECT: regional cerebral blood flow single photon emission computed tomography; ROI: region of interest obtained from AAL atlas. rAUC: ratio between areas under curve corresponding to negative and positive voxel-weights (values close to zero reflect a predominance of positive values whereas values above 1 are found in regions with predominant negative values). The words *orbitalis* and *triangularis.* were abbreviated as orb. and tri., respectively, and the words su*perior* and in*ferior* were abbreviated as sup. and inf., respectively. The brain regions that were selected in all three modalities were highlighted in dark blue. Regions that were selected in both functional modalities (¹⁸F-FDG-PET and rCBF-SPECT) were highlighted in medium blue. Regions that were selected in both T1-MRI and one of the functional modalities (either ¹⁸F-FDG-PET or CBF-SPECT) were highlighted in light blue. For each modality (T1-MRI, ¹⁸F-FDG-PET and CBF-SPECT), the selected ROIs were sorted in descending order of ROI-weight.

in regard to the considerable ROI-weight attributed to the medial temporal region, despite some differences in the exact location of the temporolimbic findings between the SPECT (parahippocampal gyrus and perirhinal cortex – BA 36 and BA 27) and PET (perirhinal cortex only – BA 36) analyses. The coincidence between MKL-ROI-based ranking profiles obtained with PET and SPECT data reinforces the validity of the spatial pattern of rCBF deficits mapped by SPECT when compared to the location of the brain metabolic abnormalities typically delineated with FDG-PET in AD patients when compared to elderly controls (Matsuda, 2007).

Since we corrected both PET and SPECT data for PVE, it is unlikely that the large ROI-weight attributed to functional abnormalities in postero-medial cortical regions and temporo-limbic structures in our study was due to PVE introduced by brain atrophy in those regions. This strengthens the view that functional neuroimaging methods applied to the diagnosis of AD provide high sensitivity to uncover localized patterns of functional hypoactivity in regions critical to the pathophysiology of AD regardless of the presence of brain atrophy in the same locations (Mevel et al., 2007).

There were important differences in regard to the labeling and

ranking of brain regions between the analyses carried out with the two atlases for PET and SPECT data. For instance, in regard to the ROI-weights attributed to medially located posterior cortical regions (precuneus and posterior cingulate gyrus), the BA atlas produced larger values for both PET and SPECT data (above 40%) compared to the AAL atlas (around 25% for PET and 29% for SPECT, respectively). Also, much larger ROI-weights were attributed to functional patterns in medial temporal cortical regions (mainly perirhinal cortex for PET, and parahippocampal plus perirhinal cortices for SPECT) when the BA atlas was used as compared to the AAL atlas (which attributed only small ROI-weights to the parahippocampal gyrus and hippocampus). In both AD and MCI, different results depending on the atlas employed have been repeatedly reported in previous ML-based studies based on the use of ROIs (Ota et al., 2015, 2014; Yao et al., 2015). This is to be expected, given their considerable differences in regard to the size and boundaries of the ROIs employed between the AAL and BA templates (Ota et al., 2014).

Despite some differences between atlases, the discrimination between AD patients and controls using the T1-MRI GM data in our study also highlighted medially located posterior cortical regions

Table 4
Regions from BA atlas selected by MKL-ROI to classify AD patients and healthy controls.

	T1-MRI			18F-FDG-PET			CBF-SPECT		
	ROI	ROI-weight (%)	rAUC	ROI	ROI-weight (%)	rAUC	ROI	ROI-weight (%)	rAUC
1	BA34 Dorsal entorhinal ctx.	17.807	3.66	BA7 Medial parietal ctx.	34.259	2.60	BA7 Medial parietal ctx.	23.471	2.30
2	BA23 Posterior cingulate gr.	16.564	1.13	BA36 Parahippocampal gr.	14.335	7.15	BA18 Secondary visual ctx.	19.052	0.22
3	BA20 Inferior temporal gr.	16.062	3.32	BA32 Dorsal anterior cingulate	9.722	4.44	BA23 Posterior cingulate gr.	15.977	6.93
4	BA22 Auditory temporal ctx.	15.951	0.98	BA23 Posterior cingulate gr.	8.683	1.93	BA27 Pyriform ctx.	13.775	6.45
5	BA4 Primary motor ctx.	8.850	0.22	BA26 Ectosplenial area	8.301	2.53	BA30 Agranular retrolimbic	9.1602	1.51
6	BA10 Anterior prefrontal ctx.	7.971	0.56	BA30 Agranular retrolimbic	7.472	0.96	BA26 - Ectosplenial area	5.3420	11.65
7	BA37 Fusiform gr.	6.312	3.09	BA17 Primary visual ctx.	5.712	0.36	BA43 Somatosensory ctx.	4.6339	0.14
8	BA45 Inferior frontal gr. (pars tri)	4.741	2.24	BA39 Angular gr.	2.691	4.84	BA39 Angular Gr.	3.1095	5.72
9	BA28 Ventral entorhinal ctx.	1.236	0.43	BA45 Inferior frontal gr. (pars tri)	2.619	3.07	BA37 Fusiform gr.	2.1893	0.67
10	BA3 Primary somatosensorial. ctx.	1.027	0.88	BA18 Secondary visual ctx.	1.750	0.25	BA32 Dorsal anterior cingulate	1.6145	13.87
11	BA7 Medial parietal ctx.	0.942	0.63	BA43 Somatosensory ctx.	1.105	0.26	BA36 Parahippocampal gr.	0.9387	6.54
12	BA38 Temporopolar area	0.899	0.35	BA35 Perihinal ctx.	0.904	1.03	BA45 Inferior frontal gr. (pars tri)	0.4814	3.10
13	BA41 Anterior transv. Temporal	0.782	2.16	BA4 Primary motor ctx.	0.685	0.11	BA3 Primary somatosensorial ctx.	0.0923	0.14
14	BA47 Frontal ctx. (pars orb.)	0.278	1.14	BA27 Pyriform ctx.	0.661	3.25	BA34 Dorsal entorhinal ctx.	0.0898	0.95
15	BA2 Posterior primary somatosens. ctx.	0.267	1.31	BA41 Anterior transv. temporal	0.321	14.88	BA35 Perihinal ctx.	0.0716	3.13
16	BA46 Dorsolateral prefrontal ctx.	0.119	1.96	BA3 Primary somatos. ctx.	0.295	0.10	BA41 Anterior transv. temporal	0.0007	0.95
17	BA42 Auditory ctx.	0.087	0.68	BA37 Fusiform gr.	0.188	1.28			
18	BA29 Granular retrosplenial ctx.	0.053	55.99	BA34 Dorsal entorhinal ctx.	0.127	1.11			
19	BA11 Orbitofrontal ctx.	0.051	0.86	BA28 Ventral entorhinal ctx.	0.112	9.33			
20				BA38 Temporopolar area	0.044	3.27			
21				BA9 Dorsolateral prefrontal ctx.	0.015	3.70			

T1-MRI: T1-weighted magnetic resonance imaging; 18F-FDG-PET: 18F-fluorodeoxyglucose-positron emission tomography; rCBF SPECT: regional cerebral blood flow single photon emission computed tomography; BA: Brodmann's area; ROI: region of interest obtained from BA atlas;. rAUC: ratio between the areas under curve corresponding to negative and positive voxel-weights (values close to zero reflect a predominance of positive values whereas values above 1 are found in regions with predominant negative values). The words *orbitalis* and *triangularis.* were abbreviated as orb. and tri., respectively, and the words *cortex* and *gyrus* were abbreviated as ctx. and gr., respectively. The brain regions that were selected in all three modalities were highlighted in dark blue. Regions that were selected in both functional modalities (18F-FDG-PET and rCBF-SPECT) were highlighted in medium blue. Regions that were selected in both T1-MRI and one of the functional modalities (either 18F-FDG-PET or rCBF-SPECT) were highlighted in light blue. For each modality (T1-MRI, 18F-FDG-PET and rCBF-SPECT), the selected ROIs were sorted in descending order of ROI-weight.
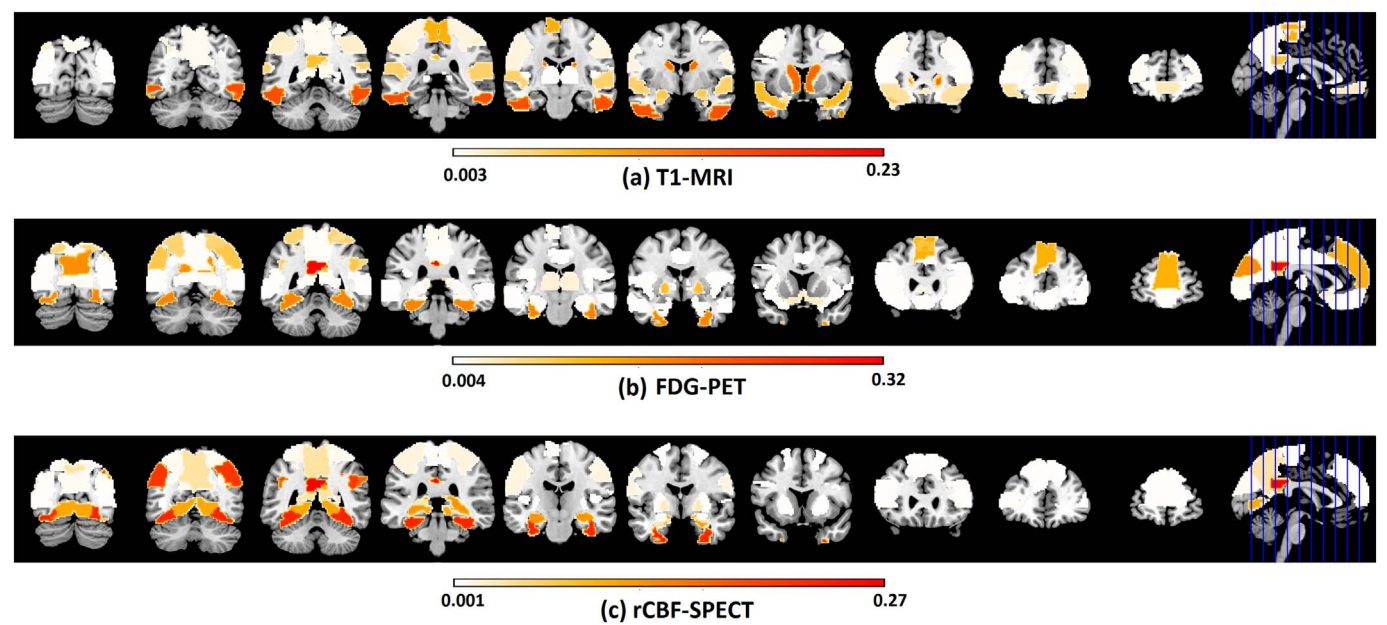

Fig. 3. ROIs from AAL atlas selected by MKL-ROI to classify AD patients and healthy controls. The regions were overlapped on a structural template and their colour varies from light yellow (minimum ROI-weight) to red (maximum ROI-weight).
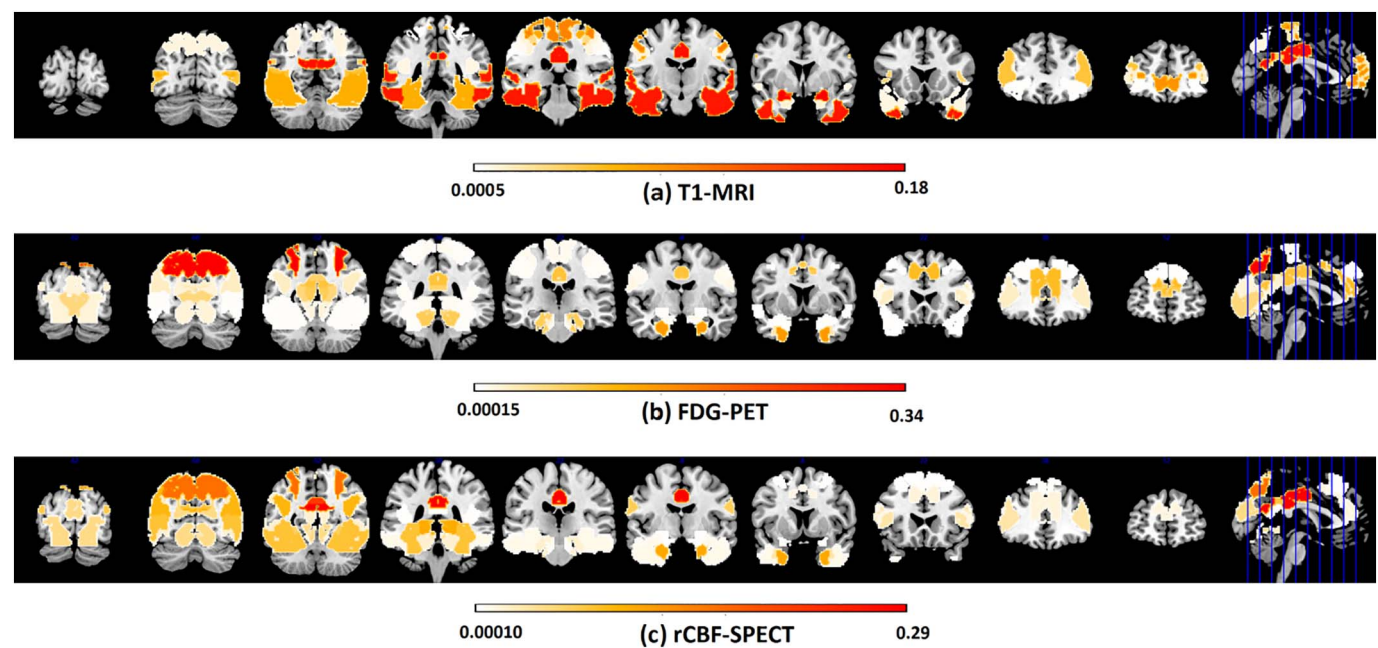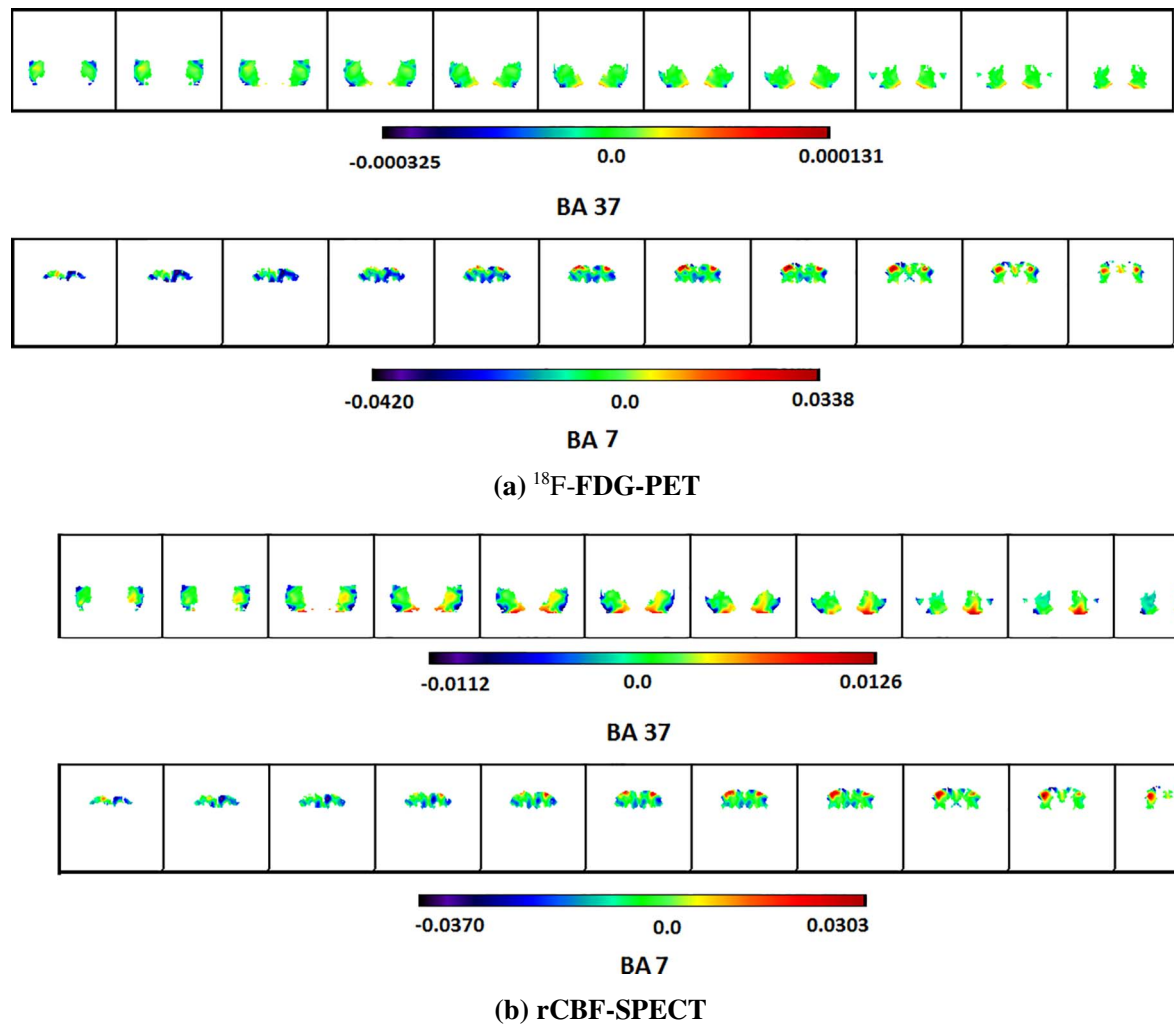
Fig. 4. ROIs from BA atlas selected by MKL-ROI to classify AD patients and healthy controls. The regions were overlapped on a structural template and their colour varies from light yellow (minimum ROI-weight) to red (maximum ROI-weight).

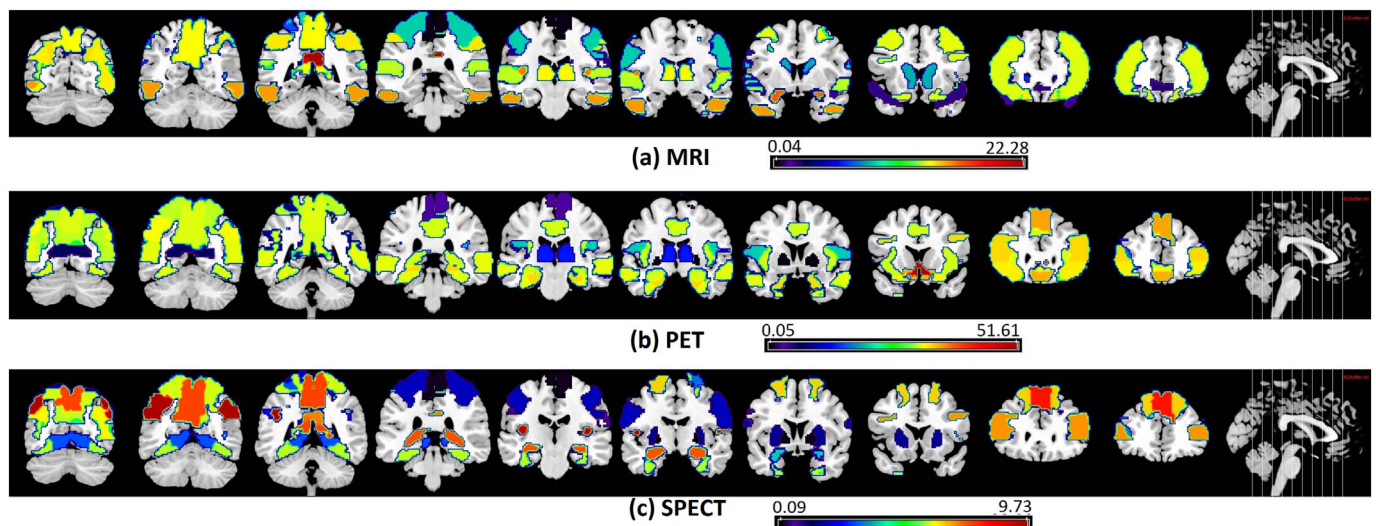**Fig. 5.** Voxel-weight in BA areas 37 and 7: (a) 18F–FDG-PET; (b) rCBF-SPECT.

Fig. 6. Predominance of signal in voxel-weights. The colours represent the rAUC (ratio between AUC- and AUC+) for each selected ROI in the AAL atlas. For clarity, rAUC was normalized independently for each modality so that cool colours (from purple to light blue) always represent rAUC < 1 (i.e., regions with predominantly positive voxel-weights). In the same way, warm colours (from yellow to red) represent rAUC > 1 (regions with predominantly negative voxel-weights) and greenish colours represent regions with rAUC close to 1 (no clear predominance of signal).

(particularly the posterior cingulate gyrus) and temporolimbic structures (mainly entorhinal cortex and inferior temporal region for the Brodmann-based analysis and the amygdala and the inferior and superior temporal gyri for the AAL-based analysis). One notable finding regarding the T1-MRI analysis regarded the greatest emphasis given to atrophy located in the lateral temporal neocortex (whichever the atlas employed), which was not highlighted in the ranking analyses for PET or SPECT data. Such T1-MRI findings are consistent with the results of previous mean group comparisons of patients with mild AD and elderly controls using voxel-based morphometry methods, which have reported prominent findings of reduced GM volume of the lateral temporal neocortex in AD (Busatto et al., 2003; Desikan et al., 2008). A high discrimination ROI-weight for lateral temporal atrophy (based on T1-MRI) not accompanied by discriminative hypoactivity in the same regions (based on PET or SPECT imaging) is an intriguing pattern that awaits replication in future investigations with larger samples.

It is important to emphasize, however, that there is a mismatch of brain structures included in each ROI across the atlases. For example, the dorsal entorhinal cortex (Brodmann area 34) received the highest weight when classifying T1 images using the Brodmann atlas (Table 4). However, there is no specific ROI delimitating the entorhinal region in the AAL atlas. The dorsal entorhinal ROI of the Brodmann atlas has a high degree of overlap with the amygdala ROI from the AAL atlas. Not surprisingly, the amygdala ROI received a high weight when classifying T1 images using the AAL atlas (Table 3). Therefore, it is possible that 1) atrophic changes in the entorhinal cortex were more precisely labelled when using the Brodmann atlas, and that 2) these changes reflected in a high weight to the amygdala ROI when using the AAL atlas. We illustrate the overlap across the atlases in these areas in Fig. S1 (supplementary material).

One novel aspect of our investigation consisted in the calculation of the rAUC, the ratio between the positive and negative voxel-weights in each selected ROI. This strategy allowed us to identify a few ROIs in which the ROI-weight of discrimination was due to a pattern of
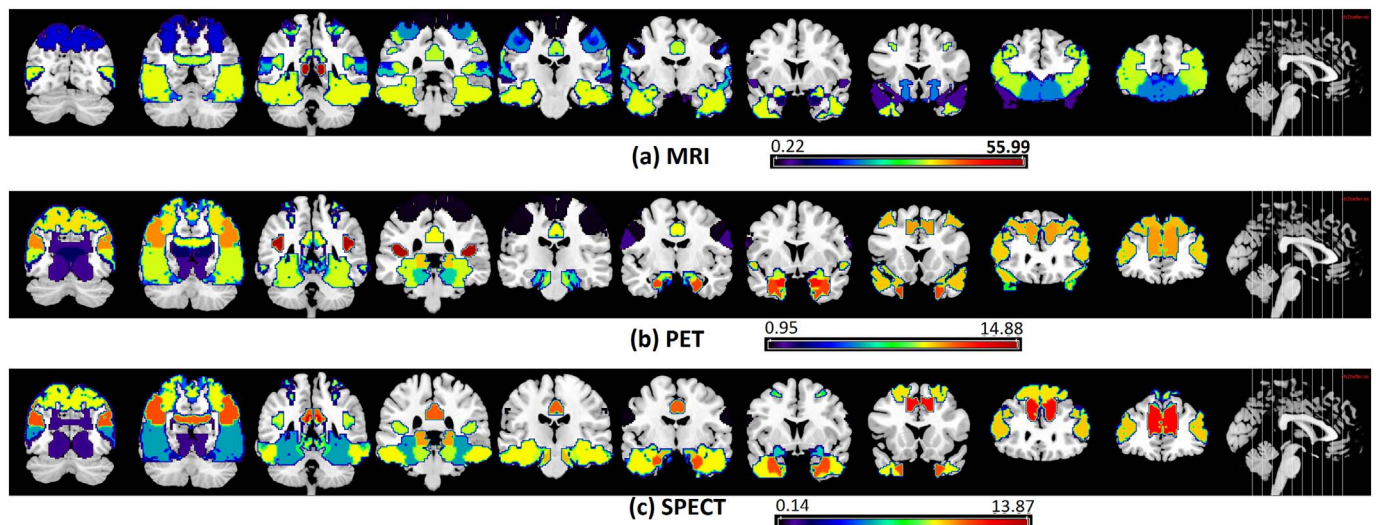

Fig. 7. Predominance of signal in voxel-weights. The colours represent the rAUC (ratio between AUC- and AUC+) for each selected ROI in the BA atlas. For clarity, rAUC was normalized independently for each modality so that cool colours (from purple to light blue) always represent rAUC < 1 (i.e., regions with predominantly positive voxel-weights). In the same way, warm colours (from yellow to red) represent rAUC > 1 (regions with predominantly negative voxel-weights) and greenish colours represent regions with rAUC close to 1 (no clear predominance of signal).

increased voxel-weight values in AD individuals present in all modalities. Surprisingly, the ROI-weights attributed to such regions were far from negligible, ranging from approximately 20% to 40% of the discrimination between AD patients and controls depending on the imaging modality. The main brain regions in which such pattern of increased voxel values in AD patients relative to controls was apparent are known to be spared by neurodegenerative AD-related processes until late stages of dementia (Busatto et al., 2003; Silverman et al., 1999; Tzourio-Mazoyer et al., 2002), including the somatosensory cortex (BA 3, BA 43), primary motor cortex (BA 4), basal ganglia, thalamus and visual cortex (BA17 and BA18). Other recent SVM investigations of FDG-PET data have reported similar findings, with the somatosensory cortex among the brain regions showing highest discrimination between MCI patients converting to AD and healthy controls (Pagani et al., 2015). Apparent functional hyperactivity in brain regions known to be spared until late stages of AD has been reported in previous PET and SPECT studies that performed mean group comparisons against elderly controls (Duran et al., 2007; Pagani et al., 2015; Soonawala et al., 2002); since the metabolic activity and cerebral blood flow in AD individuals is decreased in many GM areas, data normalization of count values in each ROI to the global tracer uptake in the brain leads to an overestimation of the relative activity measures in AD subjects in the selected brain regions that are most notably spared by the neurodegenerative AD process (Duran et al., 2007). The findings reported herein demonstrate that the classification of voxels with increased values in AD patients relative to healthy controls make an important contribution to their diagnostic discrimination when SVM-based methods are applied to PET, SPECT or T1-MRI data.

The present investigation also aimed to compare diagnostic accuracy indices obtained with the MKL-ROI approach to the indices obtained with SVM based on the whole-brain. There has been some degree of controversy in previous ML-based neuroimaging studies of AD in regard to whether greater diagnostic accuracy for the diagnosis of AD is afforded when analyses are based on whole-brain data or, instead, selected brain regions thought to be critical to the pathophysiology of AD (Cuingnet et al., 2011; Magnin et al., 2009; Pagani et al., 2015). We found some support to the latter prediction, since there was a clear increment in accuracy for PET data when applying the MKL-ROI-based method (with both the AAL and BA atlases) as compared to whole-brain findings, due to an increased ability to avoid false positives. This is a potentially relevant finding, and we argue that such accuracy increment may be explained by the large ROI-weights attributed specifically to postero-medial cortical regions in the MKL-ROI-based analyses, including the posterior cingulate gyrus (in the Brodmann-based analysis) and the precuneus (in the AAL-based analyses). It is interesting to note that such increment in diagnostic accuracy seen for ^{18}F-FDG-PET data was not obtained for rCBF SPECT data; this is consistent with the findings of recent direct comparisons that favour the use of ^{18}F-FDG-PET rather than rCBF-SPECT for the diagnosis of AD when accuracy is measured with basis on visual inspection of key brain regions by experts (O'Brien et al., 2014). When we compared the accuracy indices afforded by the two SVM methods specifically for the T1-MRI data, results were less conclusive than those for ^{18}F-FDG-PET. With MKL-ROI using the AAL atlas, the number of AD patients correctly classified did increase slightly for T1-MRI data; however, we actually found some degree of decrement in accuracy for T1-MRI data when the MKL-ROI-based method with the BA atlas was used in comparison to the whole-brain analysis, driven by a slightly lesser ability to correctly classify healthy controls as true negatives.

Limitations of the present investigation must be acknowledged, such as the modest size of the samples recruited. It is plausible to predict that greater power afforded by the use of samples of larger size would produce larger diagnostic accuracy indices than those reported herein (Frost and Kallis, 2009). On the other hand, even if modest in size, our sample was sufficient to allow a ranking profile of brain regions that is highly consistent with previous neuroimaging findings and

pathophysiological models of AD. Moreover, the MKL-ROI analysis of PET data (using either of the two atlases) produced a balanced accuracy above 90%, a measure that is highly similar to accuracy indices reported in previous studies carried out with larger samples (Zhang et al., 2011). We should also acknowledge that although we employed state-of-the-art methods to correct functional neuroimaging data for PVE, such PVE correction methodology has been validated for ^{18}F-FDG-PET rather than SPECT rCBF data.

In conclusion, the MKL-ROI approach used in the present SVM-based multimodal neuroimaging investigation highlighted brain areas of known relevance to the pathophysiology of AD (namely the posterior cingulate gyrus, precuneus and temporo-limbic cortical regions) as highly discriminative in the comparison of patients with mild AD patients versus age- and gender-matched healthy controls, particularly in the analyses carried out using functional imaging data (^{18}F–FDG-PET or rCBF SPECT). Moreover, the MKL-ROI strategy allowed us to demonstrate that voxels located in other brain regions known to be spared by AD-related neurodegenerative changes also provide substantial contribution to the SVM-based discrimination between AD and elderly control individuals, consistently across structural and functional neuroimaging modalities. Finally, while similar diagnostic accuracy indices were obtained with the MKL-ROI and whole-brain methods for T1-MRI and rCBF SPECT data, there was an increment in accuracy for the PET data when applying the MKL-ROI-based method (with both atlases), again underscoring the relevance of functional activity decrements in circumscribed posterior cortical regions as a critical imaging feature for the early diagnosis of AD.

Supplementary data to this article can be found online at https://doi.org/10.1016/j.nicl.2017.10.026.

References

American Psychiatric Association, 1987. Diagnostic and Statistical Manual of Mental Disorders, 3rd ed. The Association, Washington, DC (revised (DSM-III-R)).

Ashburner, J., 2007. A fast diffeomorphic image registration algorithm. NeuroImage 38, 95–113. http://dx.doi.org/10.1016/j.neuroimage.2007.07.007.

Ashburner, J., Friston, K.J., 2000. Voxel-based morphometry—the methods. NeuroImage 11, 805–821. http://dx.doi.org/10.1006/nimg.2000.0582.

Ashburner, J., Friston, K.J., 2005. Unified segmentation. NeuroImage 26, 839–851. http://dx.doi.org/10.1016/j.neuroimage.2005.02.018.

Boser, B.E., Guyon, I.M., Vapnik, V.N., 1992. A training algorithm for optimal margin classifiers. In: Proc. Fifth Annu. ACM Work. Comput. Learn. Theory, pp. 144–152 (doi:10.1.1.21.3818).

Braak, H., Braak, E., 1991. Neuropathological staging of Alzheimer-related changes. Acta Neuropathol. 82, 239–259. http://dx.doi.org/10.1007/BF00308809.

Brodmann, K., 1909. Vergleichende Lokalisationslehre der Großhirnrinde: in ihren Prinzipien dargestellt auf Grund des Zellenbaues.

Buchpiguel, C., Smid, J., Duran, F., Bottino, C., Ono, R., Leite, C., Busatto-Filho, G., Nitrini, R., 2014. Brain MRI, SPECT and PET in early Alzheimer's disease: a minor mismatch between volumetric and functional findings. Curr. Mol. Imaging 3, 1–9.

Busatto, G.F., Garrido, G.E., Almeida, O.P., Castro, C.C., Camargo, C.H., Cid, C.G., Buchpiguel, C.A., Furuie, S., Bottino, C.M., 2003. A voxel-based morphometry study of temporal lobe gray matter reductions in Alzheimer's disease. Neurobiol. Aging 24, 221–231.

Busatto, G.F., Diniz, B.S., Zanetti, M.V., 2008. Voxel-based morphometry in Alzheimer's disease. Expert. Rev. Neurother. 8, 1691–1702. http://dx.doi.org/10.1586/14737175.8.11.1691.

Castro, E., Gómez-Verdejo, V., Martínez-Ramón, M., Kiehl, K.A., Calhoun, V.D., 2014. A multiple kernel learning approach to perform classification of groups from complex-valued fMRI data analysis: Application to schizophrenia. NeuroImage 87, 1–17. http://dx.doi.org/10.1016/j.neuroimage.2013.10.065.

Cuingnet, R., Gerardin, E., Tessieras, J., Auzias, G., Lehéricy, S., Habert, M.O., Chupin, M., Benali, H., Colliot, O., 2011. Automatic classification of patients with Alzheimer's disease from structural MRI: A comparison of ten methods using the ADNI database.

NeuroImage 56, 766–781. http://dx.doi.org/10.1016/j.neuroimage.2010.06.013.

Curiati, P.K., Tamashiro-Duran, J.H., Duran, F.L.S., Buchpiguel, C.A., Squarzoni, P., Romano, D.C., Vallada, H., Menezes, P.R., Scazufca, M., Busatto, G.F., Alves, T.C.T.F., 2011. Age-related metabolic profiles in cognitively healthy elders: Results from a voxel-based [18*F*]fluorodeoxyglucose-positron-emission tomography study with partial volume effects correction. Am. J. Neuroradiol. 32, 560–565. http://dx.doi.org/10.3174/ajnr.A2321.

Davatzikos, C., Fan, Y., Wu, X., Shen, D., Resnick, S.M., 2008. Detection of prodromal Alzheimer's disease via pattern classification of magnetic resonance imaging. Neurobiol. Aging 29, 514–523. http://dx.doi.org/10.1016/j.neurobiolaging.2006.11.010.

Delacourte, A., David, J.P., Sergeant, N., Buée, L., Wattez, A., Vermersch, P., Ghozali, F., Fallet-Bianco, C., Pasquier, F., Lebert, F., Petit, H., Di Menza, C., 1999. The biochemical pathway of neurofibrillary degeneration in aging and Alzheimer's disease. Neurology 52, 1158–1165. http://dx.doi.org/10.1212/WNL.54.2.538.

Desikan, R.S., Fischl, B., Cabral, H.J., Kemper, T.L., Guttmann, C.R.G., Blacker, D., Hyman, B.T., Albert, M.S., Killiany, R.J., 2008. MRI measures of temporoparietal regions show differential rates of atrophy during prodromal AD. Neurology 71, 819–825. http://dx.doi.org/10.1212/01.wnl.0000320055.57329.34.

Duara, R., Loewenstein, D.A., Shen, Q., Barker, W., Potter, E., Varon, D., Heurlin, K., Vandenberghe, R., Buckley, C., 2013. Amyloid positron emission tomography with (18)F-flutemetamol and structural magnetic resonance imaging in the classification of mild cognitive impairment and Alzheimer's disease. Alzheimers Dement. 9, 295–301. http://dx.doi.org/10.1016/j.jalz.2012.01.006.

Duran, F.L.S., Zampieri, F.G., Bottino, C.C.M., Buchpiguel, C.A., Busatto, G.F., 2007. Voxel-based investigations of regional cerebral blood flow abnormalities in {Alzheimer}'s disease using a single-detector {SPECT} system. Clinics 377–384. http://dx.doi.org/10.1590/S1807-59322007000400002.

Ferreira, L.K., Busatto, G.F., 2011. Neuroimaging in Alzheimer's disease: current role in clinical practice and potential future applications. Clinics (Sao Paulo) 66 (Suppl. 1), 19–24. http://dx.doi.org/10.1590/S1807-59322011001300003.

Fox, N.C., Crum, W.R., Scahill, R.I., Stevens, J.M., Janssen, J.C., Rossor, M.N., 2001. Imaging of onset and progression of Alzheimer's disease with voxel-compression mapping of serial magnetic resonance images. Lancet 358, 201–205. http://dx.doi.org/10.1016/S0140-6736(01)05408-3.

Frost, C., Kallis, C., 2009. Reply: A plea for confidence intervals and consideration of generalizability in diagnostic studies. Brain. http://dx.doi.org/10.1093/brain/awn090.

Guo, X., Wang, Z., Li, K., Li, Z., Qi, Z., Jin, Z., Yao, L., Chen, K., 2010. Voxel-based assessment of gray and white matter volumes in Alzheimer's disease. Neurosci. Lett. 468, 146–150. http://dx.doi.org/10.1016/j.neulet.2009.10.086.

Hinrichs, C., Singh, V., Xu, G., Johnson, S., 2009. MKL for robust multi-modality AD classification. In: Lecture Notes in Computer Science (Including Subseries Lecture Notes in Artificial Intelligence and Lecture Notes in Bioinformatics), pp. 786–794. http://dx.doi.org/10.1007/978-3-642-04271-3_95.

Hirata, Y., Matsuda, H., Nemoto, K., Ohnishi, T., Hirao, K., Yamashita, F., Asada, T., Iwabuchi, S., Samejima, H., 2005. Voxel-based morphometry to discriminate early Alzheimer's disease from controls. Neurosci. Lett. 382, 269–274. http://dx.doi.org/10.1016/j.neulet.2005.03.038.

Ishii, K., 2014. PET approaches for diagnosis of dementia. AJNR Am. J. Neuroradiol. 35, 2030–2038. http://dx.doi.org/10.3174/ajnr.A3695.

Johnson, K.A., Fox, N.C., Sperling, R.A., Klunk, W.E., 2012. Brain imaging in Alzheimer disease. Cold Spring Harb. Perspect. Med. 2. http://dx.doi.org/10.1101/cshperspect.a006213.

Karas, G.B., Burton, E.J., Rombouts, S.A.R.B., Van Schijndel, R.A., O'Brien, J.T., Scheltens, P., McKeith, I.G., Williams, D., Ballard, C., Barkhof, F., 2003. A comprehensive study of gray matter loss in patients with Alzheimer's disease using optimized voxel-based morphometry. NeuroImage 18, 895–907. http://dx.doi.org/10.1016/S1053-8119(03)00041-7.

Kinkingnéhun, S., Sarazin, M., Lehéricy, S., Guichart-Gomez, E., Hergueta, T., Dubois, B., 2008. VBM anticipates the rate of progression of Alzheimer disease: A 3-year longitudinal study. Neurology 70, 2201–2211. http://dx.doi.org/10.1212/01.wnl.0000303960.01039.43.

Klöppel, S., Stonnington, C.M., Chu, C., Draganski, B., Scahill, R.I., Rohrer, J.D., Fox, N.C., Jack, C.R., Ashburner, J., Frackowiak, R.S.J., 2008. Automatic classification of MR scans in Alzheimer's disease. Brain 131, 681–689. http://dx.doi.org/10.1093/brain/awm319.

Lanckriet, G.R.G., De Bie, T., Cristianini, N., Jordan, M.I., Noble, W.S., 2004. A statistical framework for genomic data fusion. Bioinformatics 20, 2626–2635. http://dx.doi.org/10.1093/bioinformatics/bth294.

Lehmann, M., Crutch, S.J., Ridgway, G.R., Ridha, B.H., Barnes, J., Warrington, E.K., Rossor, M.N., Fox, N.C., 2011. Cortical thickness and voxel-based morphometry in posterior cortical atrophy and typical Alzheimer's disease. Neurobiol. Aging 32, 1466–1476. http://dx.doi.org/10.1016/j.neurobiolaging.2009.08.017.

Liu, F., Zhou, L., Shen, C., Yin, J., 2014. Multiple kernel learning in the primal for multimodal alzheimer's disease classification. IEEE J. Biomed. Health Inform. 18, 984–990. http://dx.doi.org/10.1109/JBHI.2013.2285378.

Magnin, B., Mesrob, L., Kinkingnéhun, S., Pélégrini-Issac, M., Colliot, O., Sarazin, M., Dubois, B., Lehéricy, S., Benali, H., 2009. Support vector machine-based classification of Alzheimer's disease from whole-brain anatomical MRI. Neuroradiology 51, 73–83. http://dx.doi.org/10.1007/s00234-008-0463-x.

Mandic, D.P., 2004. A generalized normalized gradient descent algorithm. IEEE Signal Process Lett. http://dx.doi.org/10.1109/LSP.2003.821649.

Matsuda, H., 2007. Role of neuroimaging in Alzheimer's disease, with emphasis on brain perfusion SPECT. J. Nucl. Med. 48, 1289–1300. http://dx.doi.org/10.2967/jnumed.106.037218.

Matsuda, H., 2013. Voxel-based morphometry of brain MRI in normal aging and Alzheimer's disease. Aging Dis. 4, 29–37.

Mcevoy, L.K., Fennema-notestine, C., Roddey, J.C., Holland, D., Pung, C.J., Brewer, J.B., Dale, A.M., 2009. Alzheimer disease: quantitative structural neuroimaging for detection and prediction of clinical and purpose (Methods: Results: Conclusion). Radiology 251, 195–205 (doi:2511080924 [pii]\r10.1148/radiol.2511080924).

McKhann, G., Drachman, D., Folstein, M., Katzman, R., Price, D., Stadlan, E.M., 1984. Clinical diagnosis of Alzheimer's disease: Report of the NINCDS-ADRDA Work group under the auspices of department of health and human services task force on Alzheimer's diesease. Neurology 34, 939–944.

McKhann, G.M., Knopman, D.S., Chertkow, H., Hyman, B.T., Jack, C.R., Kawas, C.H., Klunk, W.E., Koroshetz, W.J., Manly, J.J., Mayeux, R., Mohs, R.C., Morris, J.C., Rossor, M.N., Scheltens, P., Carrillo, M.C., Thies, B., Weintraub, S., Phelps, C.H., 2011. The diagnosis of dementia due to Alzheimer's disease: Recommendations from the National Institute on Aging-Alzheimer's Association workgroups on diagnostic guidelines for Alzheimer's disease. Alzheimers Dement. 7, 263–269. http://dx.doi.org/10.1016/j.jalz.2011.03.005.

Meltzer, C.C., Cantwell, M.N., Greer, P.J., Ben-Eliezer, D., Smith, G., Frank, G., Kaye, W.H., Houck, P.R., Price, J.C., 2000. Does cerebral blood flow decline in healthy aging? A PET study with partial-volume correction. J. Nucl. Med. 41, 1842–1848.

Mevel, K., Desgranges, B., Baron, J.C., Landeau, B., De la Sayette, V., Viader, F., Eustache, F., Chételat, G., 2007. Detecting hippocampal hypometabolism in Mild Cognitive Impairment using automatic voxel-based approaches. NeuroImage 37, 18–25. http://dx.doi.org/10.1016/j.neuroimage.2007.04.048.

Minoshima, S., Giordani, B., Berent, S., Frey, K.A., Foster, N.L., Kuhl, D.E., 1997. Metabolic reduction in the posterior cingulate cortex in very early Alzheimer's disease. Ann. Neurol. 42, 85–94. http://dx.doi.org/10.1002/ana.410420114.

Morris, J.C., 1993. The Clinical Dementia Rating (CDR): current version and scoring rules. Neurology 43, 2412–2414. http://dx.doi.org/10.1212/WNL.43.11.2412-a.

Morris, J.C., Storandt, M., McKeel, D.W., Rubin, E.H., Price, J.L., Grant, E.A., Berg, L., 1996. Cerebral amyloid deposition and diffuse plaques in normal aging - evidence for presymptomatic and very mild Alzheimer's disease. Neurology 46, 707–719. http://dx.doi.org/10.1212/WNL.46.3.707.

Mosconi, L., Mistur, R., Switalski, R., Tsui, W.H., Glodzik, L., Li, Y., Pirraglia, E., De Santi, S., Reisberg, B., Wisniewski, T., De Leon, M.J., 2009. FDG-PET changes in brain glucose metabolism from normal cognition to pathologically verified Alzheimer's disease. Eur. J. Nucl. Med. Mol. Imaging 36, 811–822. http://dx.doi.org/10.1007/s00259-008-1039-z.

Mosconi, L., Berti, V., Glodzik, L., Pupi, A., De Santi, S., De Leon, M.J., 2010. Pre-clinical detection of Alzheimer's disease using FDG-PET, with or without amyloid imaging. J. Alzheimers Dis. http://dx.doi.org/10.3233/JAD-2010-091504.

Mourão-Miranda, J., Portual, L., Rondina, J.M., Shawe-Taylor, J., 2012. Elastic-net Multiple Kernel Learning for multi-region neuroimaging-based diagnosis. In: Proceedings of the 2nd NIPS Workshop on Machine Learning and Interpretation in Neuroimaging, pp. 1–8. http://dx.doi.org/10.13140/RG.2.1.5137.7365.

Nadkarni, N.K., Levy-Cooperman, N., Black, S.E., 2012. Functional correlates of instrumental activities of daily living in mild Alzheimer's disease. Neurobiol. Aging 33, 53–60. http://dx.doi.org/10.1016/j.neurobiolaging.2010.02.001.

Nordberg, A., Rinne, J.O., Kadir, A., Långström, B., 2010. The use of PET in Alzheimer disease. Nat. Rev. Neurol. 6, 78–87. http://dx.doi.org/10.1038/nrneurol.2009.217.

O'Brien, J.T., Firbank, M.J., Davison, C., Barnett, N., Bamford, C., Donaldson, C., Olsen, K., Herholz, K., Williams, D., Lloyd, J., 2014. 18F-FDG PET and perfusion SPECT in the diagnosis of Alzheimer and Lewy body dementias. J. Nucl. Med. 55, 1959–1965. http://dx.doi.org/10.2967/jnumed.114.143347.

Ortiz, A., Górriz, J.M., Ramírez, J., Martinez-Murcia, F.J., 2014. Automatic ROI selection in structural brain MRI using SOM 3D projection. PLoS One 9. http://dx.doi.org/10.1371/journal.pone.0093851.

Ota, K., Oishi, N., Ito, K., Fukuyama, H., 2014. A comparison of three brain atlases for MCI prediction. J. Neurosci. Methods 221, 139–150. http://dx.doi.org/10.1016/j.jneumeth.2013.10.003.

Ota, K., Oishi, N., Ito, K., Fukuyama, H., 2015. Effects of imaging modalities, brain atlases and feature selection on prediction of Alzheimer's disease. J. Neurosci. Methods 256, 168–183. http://dx.doi.org/10.1016/j.jneumeth.2015.08.020.

Pagani, M., De Carli, F., Morbelli, S., Öberg, J., Chincarini, A., Frisoni, G.B., Galluzzi, S., Perneczky, R., Drzezga, A., Van Berckel, B.N.M., Ossenkoppele, R., Didic, M., Guedj, E., Brugnolo, A., Picco, A., Arnaldi, D., Ferrara, M., Buschiazzo, A., Sambuceti, G., Nobili, F., 2015. Volume of interest-based [18*F*]fluorodeoxyglucose PET discriminates MCI converting to Alzheimer's disease from healthy controls. A European Alzheimer's Disease Consortium (EADC) study. NeuroImage Clin. 7, 34–42. http://dx.doi.org/10.1016/j.nicl.2014.11.007.

Pereira, J.M.S., Xiong, L., Acosta-Cabronero, J., Pengas, G., Williams, G.B., Nestor, P.J., 2010. Registration accuracy for VBM studies varies according to region and degenerative disease grouping. NeuroImage 49, 2205–2215. http://dx.doi.org/10.1016/j.neuroimage.2009.10.068.

Petersen, R.C., Aisen, P.S., Beckett, L.A., Donohue, M.C., Gamst, A.C., Harvey, D.J., Jack, C.R., Jagust, W.J., Shaw, L.M., Toga, A.W., Trojanowski, J.Q., Weiner, M.W., 2010. Alzheimer's Disease Neuroimaging Initiative (ADNI): clinical characterization. Neurology 74, 201–209. http://dx.doi.org/10.1212/WNL.0b013e3181cb3e25.

Quarantelli, M., Berkouk, K., Prinster, A., Landeau, B., Svarer, C., Balkay, L., Alfano, B., Brunetti, A., Baron, J.-C., Salvatore, M., 2004. Integrated software for the analysis of brain PET/SPECT studies with partial-volume-effect correction. J. Nucl. Med. 45, 192–201.

Rakotomamonjy, A., Bach, F.R., Canu, S., Grandvalet, Y., 2008. SimpleMKL. J. Mach. Learn. Res. 9, 2491–2521.

Ritter, K., Schumacher, J., Weygandt, M., Buchert, R., Allefeld, C., Haynes, J.-D., 2015. Multimodal prediction of conversion to Alzheimer's disease based on incomplete

biomarkers. Alzheimer's Dement. Diagn. Assess. Dis. Monit. 1, 206–215. http://dx.doi.org/10.1016/j.dadm.2015.01.006.

Rondina, J., Hahn, T., de Oliveira, L., Marquand, A., Dresler, T., Leitner, T., Fallgatter, A., Shawe-Taylor, J., Mourao-Miranda, J., 2013. SCoRS - a method based on stability for feature selection and mapping in neuroimaging. IEEE Trans. Med. Imaging 33, 85–98. http://dx.doi.org/10.1109/TMI.2013.2281398.

Rorden, C., Brett, M., 2000. Stereotaxic Display of Brain Lesions. Behav. Neurol. 12, 191–200. http://dx.doi.org/10.1155/2000/421719.

Ruan, Q., D'Onofrio, G., Sancarlo, D., Bao, Z., Greco, A., Yu, Z., 2016. Potential neuroimaging biomarkers of pathologic brain changes in Mild Cognitive Impairment and Alzheimer's disease: a systematic review. BMC Geriatr. 16, 104. http://dx.doi.org/10.1186/s12877-016-0281-7.

Schrouff, J., Rosa, M.J., Rondina, J.M., Marquand, A.F., Chu, C., Ashburner, J., Phillips, C., Richiardi, J., Mourão-Miranda, J., 2013. PRoNTo: Pattern recognition for neuroimaging toolbox. Neuroinformatics 11, 319–337. http://dx.doi.org/10.1007/s12021-013-9178-1.

Ségonne, F., Dale, A.M., Busa, E., Glessner, M., Salat, D., Hahn, H.K., Fischl, B., 2004. A hybrid approach to the skull stripping problem in MRI. NeuroImage 22, 1060–1075. http://dx.doi.org/10.1016/j.neuroimage.2004.03.032.

Silverman, D.H.S., 2004. Brain 18 F-FDG PET in the diagnosis of neurodegenerative dementias: comparison with perfusion spect and with clinical evaluations lacking nuclear imaging. J. Nucl. Med. 45, 594–607.

Silverman, D.H.S., Small, G.W., Phelps, M.E., 1999. Clinical value of neuroimaging in the diagnosis of dementia. Sensitivity and specificity of regional cerebral metabolic and other parameters for early identification of Alzheimer's disease. Clin. Positron Imaging 2, 119–130 (doi:Export Date 16 July 2013\rSource Scopus).

Sled, J.G., Zijdenbos, A.P., Evans, A.C., 1998. A nonparametric method for automatic correction of intensity nonuniformity in MRI data. IEEE Trans. Med. Imaging 17, 87–97. http://dx.doi.org/10.1109/42.668698.

Smith, S.M., 2002. Fast robust automated brain extraction. Hum. Brain Mapp. 17, 143–155. http://dx.doi.org/10.1002/hbm.10062.

Soonawala, D., Amin, T., Ebmeier, K., Steele, J., Dougall, N., Best, J., Migneco, O., Nobili, F., Scheidhauer, K., 2002. Statistical parametric mapping of (99 m)Tc-HMPAO-SPECT images for the diagnosis of Alzheimer's disease: normalizing to cerebellar tracer uptake. NeuroImage 17, 1193–1202.

Thompson, P.M., Hayashi, K.M., De Zubicaray, G.I., Janke, A.L., Rose, S.E., Semple, J., Hong, M.S., Herman, D.H., Gravano, D., Doddrell, D.M., Toga, A.W., 2004. Mapping hippocampal and ventricular change in Alzheimer disease. NeuroImage 22, 1754–1766. http://dx.doi.org/10.1016/j.neuroimage.2004.03.040.

Tzourio-Mazoyer, N., Landeau, B., Papathanassiou, D., Crivello, F., Etard, O., Delcroix, N., Mazoyer, B., Joliot, M., 2002. Automated anatomical labeling of activations in SPM using a macroscopic anatomical parcellation of the MNI MRI single-subject brain. NeuroImage 15, 273–289. http://dx.doi.org/10.1006/nimg.2001.0978.

Vapnik, V.N., 1998. Statistical Learning Theory. John Wiley & Sonshttp://dx.doi.org/10.2307/1271368.

Vemuri, P., Wiste, H.J., Weigand, S.D., Knopman, D.S., Trojanowski, J.Q., Shaw, L.M., Bernstein, M.A., Aisen, P.S., Weiner, M., Petersen, R.C., Jack, C.R., 2010. Serial MRI and CSF biomarkers in normal aging, MCI, and AD. Neurology 75, 143–151. http://dx.doi.org/10.1212/WNL.0b013e3181e7ca82.

Xia, Y., Lu, S., Wen, L., Eberl, S., Fulham, M., Feng, D.D., 2014. Automated identification of dementia using FDG-PET imaging. Biomed. Res. Int. 2014. http://dx.doi.org/10.1155/2014/421743.

Yao, Z., Hu, B., Xie, Y., Moore, P., Zheng, J., 2015. A review of structural and functional brain networks: small world and atlas. Brain Inform. 2, 45–52. http://dx.doi.org/10.1007/s40708-015-0009-z.

Zhang, D., Wang, Y., Zhou, L., Yuan, H., Shen, D., 2011. Multimodal classification of Alzheimer's disease and mild cognitive impairment. NeuroImage 55, 856–867. http://dx.doi.org/10.1016/j.neuroimage.2011.01.008.